Inverter and Battery Drive Cycle Efficiency Comparisons of CHB and MMSP Traction Inverters for Electric Vehicles

Inverter and Battery Drive Cycle Efficiency Comparisons of CHB and MMSP Traction Inverters for Electric Vehicles

Anton Kersten[1], Manuel Kuder[2], Emma Grunditz[1], Zeyang Geng[1], Evelina Wikner[1], Torbjörn Thiringer[1], Thomas Weyh[2], and Richard Eckerle[2]

[1]Chalmers University of Technology, Gothenburg, Sweden
Email: kersten@chalmers.se
[2]University of the German Federal Armed Forces, Munich, Germany
Email: manuel.kuder@unibw.de

September 2019

Keywords
≪Battery≫, ≪Cascaded≫, ≪Conduction losses≫, ≪Efficiency≫, ≪Electric vehicle≫, ≪H-bridge≫ ≪IGBT≫, ≪MOSFET≫, ≪Multilevel converter≫, ≪Multilevel system≫, ≪Switching losses≫.

Abstract
This papers investigates the performance of several inverter types for electric vehicles. A standard two-level and two seven-level multilevel inverters, a cascaded H-bridge (CHB) and a modular multilevel series parallel (MMSP) inverter, are considered. Based on the AC impedance spectra measured on a single battery cell, the battery pack impedances of the multilevel and two-level inverter systems are modeled. The inverter losses are modeled using the semiconductors' datasheets. Based on the loss models, the inverter and battery efficiency during different driving cycles are assessed. In comparison to the two-level inverter system, the multilevel inverter drivetrains show an increased drivetrain efficiency, despite increased battery losses. The MMSP topology showed the best result. In comparison to the CHB topology, the battery losses were reduced by the MMSP inverter system.

Introduction
In vehicle-traction applications the two-level inverter typology is widely spread and vastly used, due to its maturity [1, 2]. However, emerging multilevel inverter topologies offer several advantages compared to common two-level inverters regarding drive cycle efficiency [3, 4, 5], especially in partial load operation [6, 7], low-order harmonic and EMI emissions [8], and redundant operation during fault condition [9]. Nevertheless, the disadvantages are an increased control effort and an increased system complexity.

In [7], the drive cycle efficiency of a cascaded H-bridge (CHB) multilevel inverter, based on low voltage MOSFETs, is compared with a two-level inverter using silicon carbide MOSFETs or IGBTs. Within this investigation, the CHB inverter shows the best drive cycle efficiency, but the battery losses are neglected. A similar drive cycle comparison can be found in [10], where a battery and inverter loss comparison of a CHB and modular multilevel series parallel (MMSP) converter is carried out. However, in their investigation, the reverse conduction of the MOSFETs, as described in [11], is not considered, the battery modeling is simplified, the generator operation is not distinguished from the motor operation, and the voltage level of the DC-link and output voltage is unreasonably varied for the different inverter topologies.

Therefore, this paper shows a fair drive cycle comparison of a two-level inverter, utilizing IGBTs or MOSFETs, and two seven-level multilevel inverters, a cascaded H-bridge (CHB) and a modular multilevel series parallel (MMSP) inverter, using low voltage MOSFETs. For the analysis the reverse conduction of the MOSFETs is considered, generator and motor operation are distinguished and the battery packs are modeled, based on measurements performed on a single battery cell, according to the Randles model with three RC-elements [12]. Furthermore, the battery and the inverter losses are separately quantified.

Inverter Topologies

The classical two-level inverter system is supplied by one battery pack and one half-bridge is used for each phase, as shown in Fig. 1(a). The CHB and the MMSP converter consist of several series connected sub-modules per phase as shown in Fig. 1(b) [10, 13]. In the CHB converter, the battery modules can be individually bypassed or inserted in forward and reverse direction, and the MMSP converter can additionally parallelize the battery packs in each phase, if the desired output voltage is low. In this manner, the overall battery losses can be reduced by the MMSP topology, which is beneficial at low speeds.

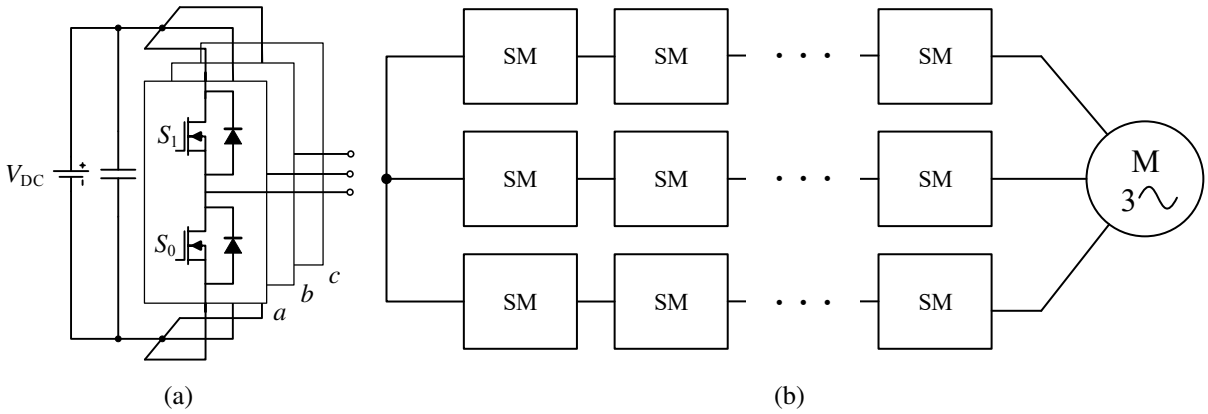

Fig. 1: (a) Classical two-level inverter topology and (b) structure of the CHB/MMSP topology.

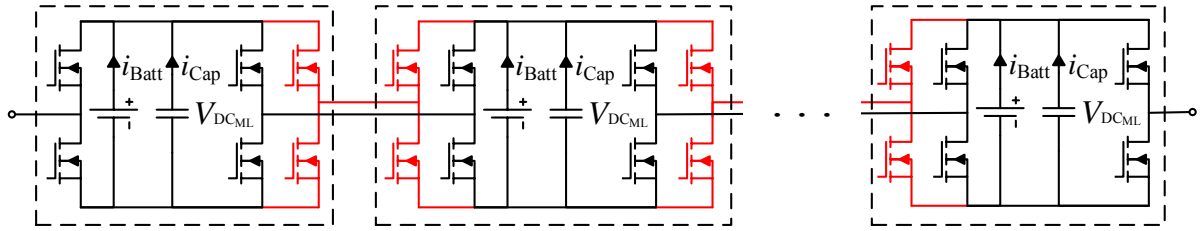

Fig. 2: CHB inverter submodules and additional half-bridges of the MMSP topology marked in red.

Modeling Battery Losses

The battery pack's impedance can be modeled as described in [12], using a three time constant model with a series inductance and resistance. Consequently, the impedance network with a parallel DC-link capacitor can be modeled as shown in Fig. 3. Using the simulated DC-link current, the ohmic battery losses can be determined by the voltage drop across the resistances, including the capacitor's equivalent series resistance R_{ESR}. For the calculation of the battery pack impedances a reference battery cell was

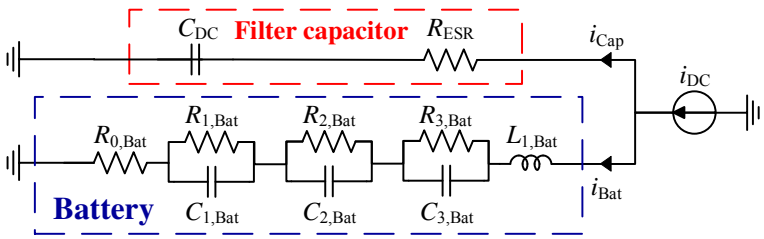

Fig. 3: Battery impedance network with parallel capacitor and injected DC link current [12].

used. The cylindrical, 18650 high-energy cell chosen is manufactured by LG Chem. It has a nominal voltage of 3.72 V and a rated capacity of 2800 mAh, which corresponds to about 10.42 Wh [14]. The impedance of the cell was determined at room temperature using an AC impedance-spectroscopy, as

shown in Fig. 4. Different state of charge (SOC) conditions and a frequency range from 10 mHz to 10 kHz were considered. A least-square approach was used to extract the cell parameters for a characteristic SOC of 50 %, which are shown in Table I. From Fig. 4(b) it can be seen that the chosen parameters comply with the measured impedance within a frequency range from a couple of hundred mHz to 4 kHz.

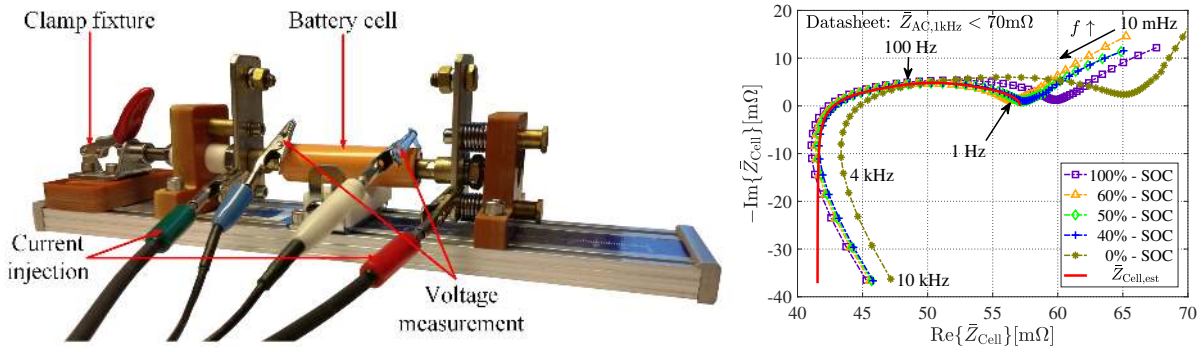

(a) (b)

Fig. 4: (a) Battery cell test fixture and (b) impedance plot of the high energy cell for different SOCs.

Table I: Battery cell parameters

R0 [mΩ]	R1 [mΩ]	R2 [mΩ]	R3 [mΩ]	C1 [mF]	C2 [mF]	C3 [F]	L [nH]
41.53	5.02	7.32	3.23	75.44	339.5	3.625	590.8

Modeling Inverter Losses

The switching and conduction losses of the used IGBTs and MOSFETs are modeled using a lookup-table approach, as described in [4] ,using datasheet values. The datasheet switching losses of the IGBTs are scaled according to [15] as

$$E_{\mathrm{switch}} = E_{\mathrm{nom}} \cdot \left(\frac{i}{i_{\mathrm{nom}}}\right)^{K_{\mathrm{i}}} \cdot \left(\frac{V_{\mathrm{DC}}}{V_{\mathrm{nom}}}\right)^{K_{\mathrm{v}}} \text{ with } \begin{cases} K_{\mathrm{i,IGBT}} \simeq 1,\ K_{\mathrm{i,Diode}} \simeq 0.6 \\ K_{\mathrm{v,IGBT}} \simeq 1.3 \ldots 1.4,\ K_{\mathrm{v,Diode}} \simeq 0.6 \end{cases} \tag{1}$$

The junction temperatures T_{J} of the semiconductors are modeled using a thermal RC-network, as shown in Fig. 5. Assuming an equal loss distribution among the switches, the thermal resistance $R_{\mathrm{th,JS}}$ can be divided by the number of switches N_{Sw}. A cooling plate is used as a heatsink, modeled by an RC element. The coolant's temperature can vary, depending on the flow velocity and the ambient temperature, within a range from 50 °C up to 85 °C [15].

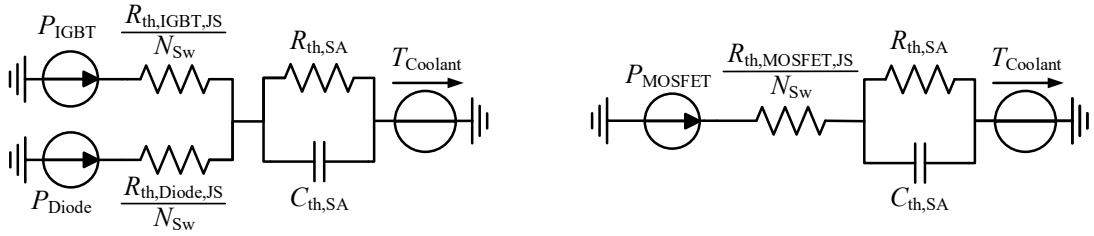

(a) (b)

Fig. 5: Thermal model of the (a) IGBT inverter, including antiparallel diodes, and (b) the MOSFET inverter.

Motor and Vehicle Dynamics

The electromagnetic torque of an interior permanent magnet machine is dependent on the inductance difference in dq-reference and the magnetic constant ψ_{m}, as can be described as

$$T_{\mathrm{elec}} = \frac{3n_{\mathrm{p}}}{2}\left[(L_{\mathrm{d}} - L_{\mathrm{q}})i_{\mathrm{d}}i_{\mathrm{q}} + \psi_{\mathrm{m}}i_{\mathrm{q}}\right] \tag{2}$$

The motor's currents can be controlled using an MTPA and MTPV control strategy or these can be controlled, as described in [16, 17], to account for the nonlinearities of the electric motor in order to achieve an optimal motor efficiency. At steady state, a torque equilibrium of the electrical (T_e) and mechanical torque (T_m) is achieved. Therefore, the gearbox ratio and the gearbox's efficiency can be considered as

$$T_\mathrm{e} = T_\mathrm{m} = \frac{T_\mathrm{wheel}}{G_\mathrm{r}\eta_\mathrm{G}^{\mathrm{sgn}(T_\mathrm{wheel})}} \tag{3}$$

$$\frac{\omega_\mathrm{e}}{n_\mathrm{p}} = \omega_\mathrm{motor} = \omega_\mathrm{r} = \omega_\mathrm{wheel} G_\mathrm{r} \tag{4}$$

Here, the torque, acting on the wheels, can be calculated by the product of the sum of forces acting on the car and the wheels' radius as

$$T_\mathrm{wheel} = r_\mathrm{wheel} F_\mathrm{net} \tag{5}$$

The overall forces acting on the vehicle in longitudinal direction consists of the sum of the rolling/friction resistance, aero dynamic drag, road gradient and acceleration force as

$$F_\mathrm{net} = F_\mathrm{rolling} + F_\mathrm{aero} + F_\mathrm{gradient} + F_\mathrm{acceleration} \tag{6}$$

$$F_\mathrm{acceleration} = (m_\mathrm{veh} + m_\mathrm{occ})\, a \tag{7}$$

$$F_\mathrm{airdrag} = 0.5\ \rho_\mathrm{air}\ C_\mathrm{d}\ v^2\ A \tag{8}$$

$$F_\mathrm{rolling} = (m_\mathrm{veh} + m_\mathrm{occ})\ g\ C_\mathrm{r}\ \cos(\alpha) \tag{9}$$

$$F_\mathrm{gradient} = (m_\mathrm{veh} + m_\mathrm{occ})\ g\ \sin(\alpha) \tag{10}$$

Fig. 6(a) shows four different driving cycles, resembling typical vehicle loads for city driving (FTP-75),

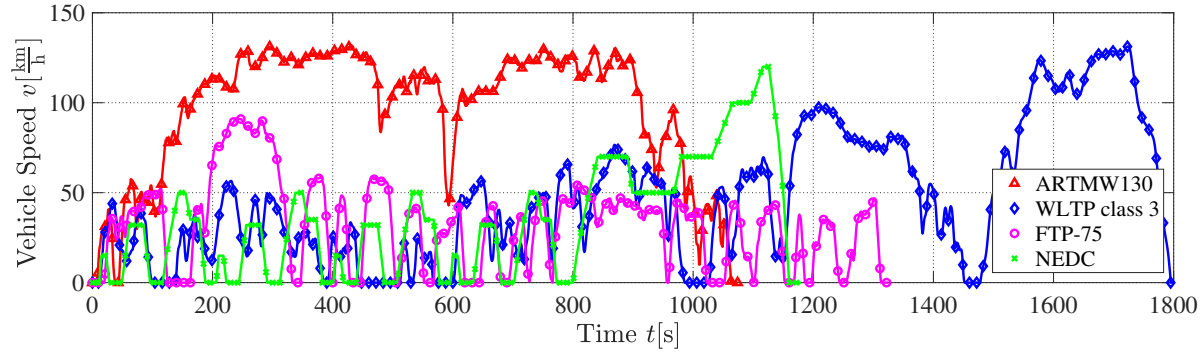

(a)

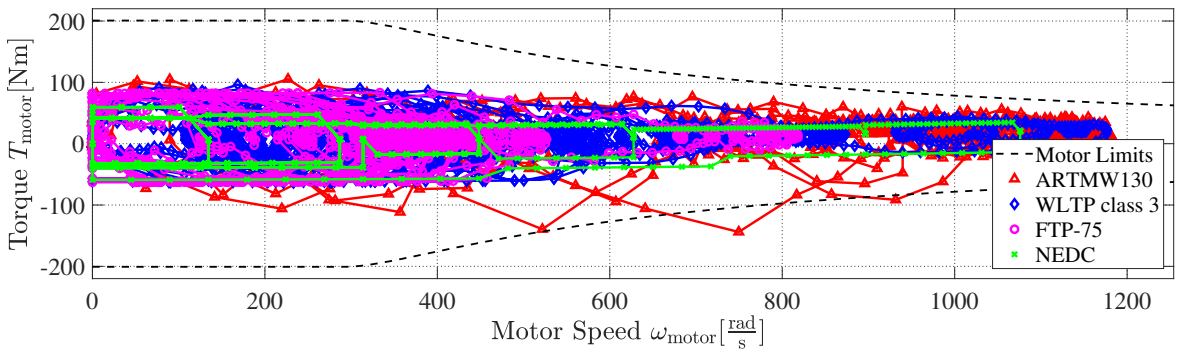

(b)

Fig. 6: (a) Driving cycles and (b) the corresponding motor operating points for a small passenger vehicle.

highway driving (ARTMW130) and test procedure driving (WLTP, NEDC). In Fig. 6(b) the resulting motor operating points, calculated from (3) to (10), are depicted.

Case Setups and Drive Cycle Simulation

Drivetrain Setups

For the simulation case setup, a small passenger car driven by an interior permanent magnet machine is considered. The chosen vehicle and motor parameters are shown in Table II. The reference two-

Table II: Passenger car and motor model parameters

(a) Vehicle

	Value	Unit
Vehicle mass m_{veh}	1500	kg
Occupant weight m_{occ}	75	kg
Frontal area A	2.2	m^2
Drag cofficient C_{d}	0.30	
Rolling resistance C_{r}	0.012	
Wheel radius r_{wheel}	0.316	m
Gear box ratio G_{r}	10.2	
Gearbox efficiency η_{G}	95	%
Top speed v_{max}	140	km/h

(b) Motor

	Value	Unit
Stator resistance R_{s}	20	mΩ
D-axis inductance L_{d}	250	µH
Q-axis inductance L_{q}	700	µH
Flux constant ψ_{m}	75	mWb
Pole pairs n_{p}	4	
Max torque T_{max}	200	Nm
Max phase current I_{RMS}	190	A
Max phase voltage $\hat{V}_{\text{Peak}}$	200	V
Max speed n	12000	rpm

level inverter system comprises a 400 V battery with an overall battery capacity of about 45 kWh. The number of submodules m per phase of the CHB and MMSP inverter is chosen to be three, achieving seven voltage levels per phase. To achieve the desired inverter output voltage, space vector modulation is used for the two and the seven-level inverters, using a switching frequency of f_{sw} =10 kHz. Thus, the nominal battery pack voltage of the multilevel inverters can be scaled relative to the battery system of the two-level inverter as

$$V_{\text{Bat,ML}} = \frac{V_{\text{Bat,2L}}}{2m} = 66.6\,\text{V} \tag{11}$$

and the battery pack capacity as

$$C_{\text{Bat,ML}} = \frac{C_{\text{Bat,2L}}}{3m} = 5\,\text{kWh} \tag{12}$$

The number of series battery cells of the 400 V reference battery can be easily calculated as

$$n_{\text{s,2L}} = \frac{400\,\text{V}}{3.72\,\text{V}} = 108 \tag{13}$$

Thus, the overall number of battery cells can be obtained by the capacity as

$$n_{\text{cells,2L}} = \frac{45\,\text{kW}h}{10.42\,\text{Wh}} = 4319 \rightarrow 4320 \tag{14}$$

which gives a number of parallel strands as $n_{\text{p,2L}} = 40$. Consequently, the number of parallel and series cells for one battery pack of the CHB and MMSP converter can be calculated in a similar manner as follows:

$$n_{\text{s,ML}} = \frac{66.6\,\text{V}}{3.72\,\text{V}} = 18 \tag{15}$$

$$n_{\text{p,ML}} = \frac{n_{\text{cells,2L}}}{3m \cdot n_{\text{s,ML}}} = \frac{4320}{9 \cdot 18} = 27 \tag{16}$$

From the series and parallel cells, the battery pack impedance of the two-level and the multilevel can be calculated with respect to a single battery cell as:

$$Z_{2L} = \frac{n_{s,2L}}{n_{p,2L}} Z_{cell} = N_{B,2L} Z_{cell} = 2.7 \cdot Z_{cell} \tag{17}$$

$$Z_{ML} = \frac{n_{s,ML}}{n_{p,ML}} Z_{cell} = N_{B,ML} Z_{cell} = 0.66 \cdot Z_{cell} \tag{18}$$

The chosen DC link capacitor of the two-level inverter, as analysed in [18], has an $R_{ESR} = 2.5\,\mathrm{m\Omega}$ and a capacitance of $C_{DC} = 540\,\mu\mathrm{F}$. For the multilevel inverters, the single DC link capacitors of each sub-module are chosen in accordance to the energy density of the reference system as

$$C_{DC,ML} = C_{DC,2L} \frac{V_{Bat,2L}^2}{V_{Bat,ML}^2} \rightarrow C_{DC,ML} = 540\,\mu\mathrm{F} \frac{(400\,\mathrm{V})^2}{(66\,\mathrm{V})^2} = 20\,\mathrm{mF} \tag{19}$$

Therefore, 20 aluminium electrolyte capacitors with an individual capacity of 1 mF [19] are connected in parallel per H-bridge. The chosen water-cooled heatsink for all inverters can be found in [20]. According to the datasheet, the thermal resistance at a water flow rate of 0.5 GPM is $R_{th,SA} = 0.016\,\mathrm{K\,W^{-1}}$. The thermal capacity of the heatsink is estimated by the volume of it and the specific heat capacity of aluminium as

$$C_{th,SA} = \frac{V_{plate,Al} \rho_{Al}}{c_{Al}} = 0.247\,\mathrm{W\,h\,K^{-1}} \tag{20}$$

The chosen semiconductor switches for the two-level and multilevel inverter drivetrainss are presented in Table III. For the two-level inverter an IGBT and a MOSFET solution are chosen, while the chosen MOSFETs can be just operated with antiparallel Schottky Diodes to lower the reverse recovery losses to a reasonable extent.

Table III: Chosen inverter semiconductor switches

Inverter	Switch	Type	$V_{blocking}$	I_{nom}	N	PPU	Cost
2-level	FS400R07A3E3 [21]	IGBT	700 V	400 A	6	341.54 €[1]	341.54 €
2-level[3]	FCH023N65S3L4 [22]	MOSFET	650 V	65.8 A	30	6.56 €[2]	196.8 €
	C5D5006584 [23]	Schottky Diode	650 V	50 A	30	16.11 €[2]	483.3 €
CHB	IPT015N10N5 [24]	MOSFET	100 V	300 A	36	3.37 €[2]	121.32 €
MMSP	IPT015N10N5 [24]	MOSFET	100 V	300 A	60	3.37 €[2]	202.20 €

[1] price for entire IGBT module for purchase of at least 5 units, [2] price for purchase of at least 1000 units,
[3] must be operated with antiparallel Schottky Diode

Simulation of Drivetrain Losses and Drive Cycle Performance

The drive cycle losses are estimated using two main steps, the loss calculation of the inverter and the battery losses, and the drive cycle analysis, as schematically depicted in Fig. 7. This approach is chosen, since a complete simulation of a driving cycle would require a very high time resolution to include every switching event, which in turn requires extensive computational memory. Therefore, at first, the battery and inverter losses for the entire operating range of the drivetrains are determined with the software tools MATLAB Simulink and Plexim's PLECS. A temperature dependence of the inverter losses is considered and the losses are determined for a junction temperature range from 50 °C to 100 °C using a stepsize of 10 K. Regarding the battery, it is assumed that the battery impedance is constant throughout the driving cycles, since the battery's thermal time constant is much larger than the driving cycles' durations and the drawn energy during a driving cycle does not essentially alter the SOC of the battery. After obtaining the loss maps, a lookup table approach is used to determine the drive cycle losses. With the given speed and acceleration profile of the corresponding driving cycle, the operating point of the drivetrains can be calculated using MATLAB Simulink. Using the previously created loss maps, the inverter and battery

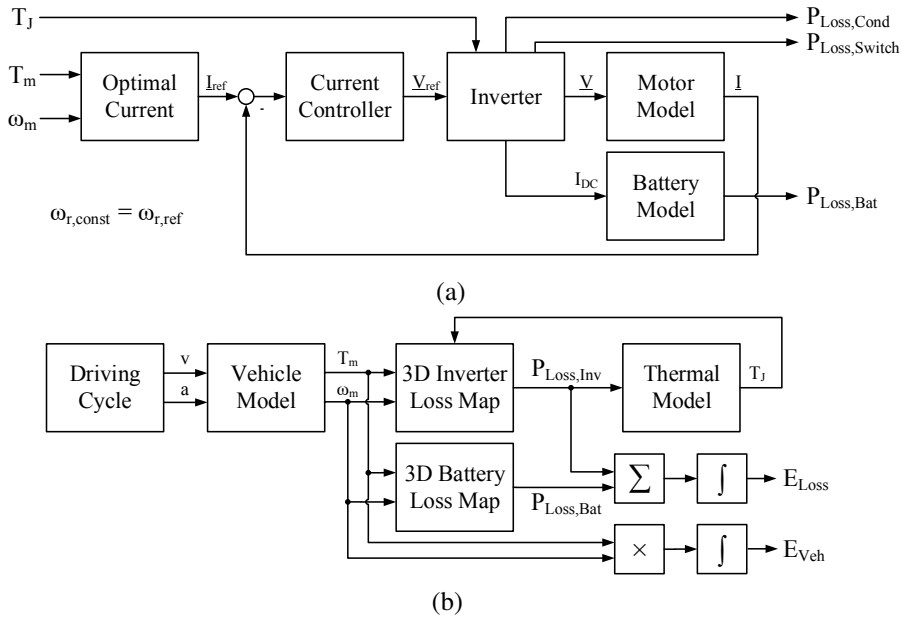

Fig. 7: Schematic of (a) the battery and inverter loss simulation, and (b) the drive cycle analysis.

losses can be determined for each time instant of the driving cycle.

Drive Cycle Evaluation

Drivetrain Efficiency

As mentioned before, the battery and inverter losses of the different drive systems are first obtained from simulations for the entire operating range of the drivetrain. Fig. 8 depicts the battery efficiency of the two-level inverter system, determined by the battery losses of the IGBT or MOSFET solution. The battery efficiency reduces with increasing speed and increasing motor torque. In comparison to that, Fig. 9

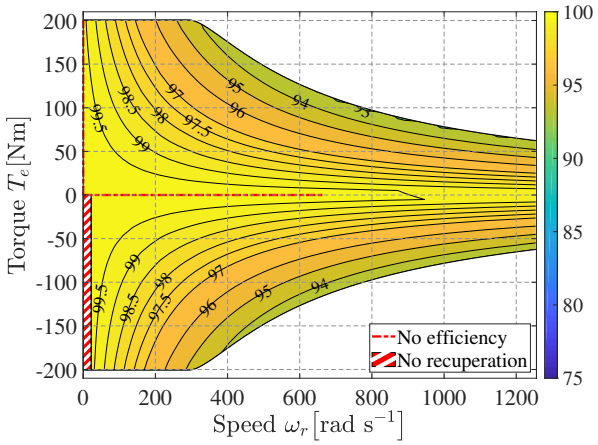

Fig. 8: Battery efficiency map for the two-level IGBT or MOSFET inverter system.

shows the battery efficiency of the CHB and MMSP inverters, respectively. Since the motor currents are intermittently conducted through the battery packs, the CHB inverter's battery system shows a reduced efficiency, especially below rated speed. In comparison to the CHB inverter, the MMSP inverter reduces the losses below rated speed, whereas the losses at high speed are just marginally reduced. Since the battery impedance per phase is varying with the modulation index, the isopotential lines of the efficiency are not as smooth as for the two-level inverter system. From the efficiency maps, it is seen that the two-level inverter shows the lowest battery losses at any operating point.

Fig. 10 shows an excerpt of the efficiency maps of the considered inverters for a junction temperature of 70 °C. The multilevel inverters show a high efficiency at partial loading and low speed. Furthermore, their peak efficiency is increased in comparison to the IGBT and MOSFET two-level in-

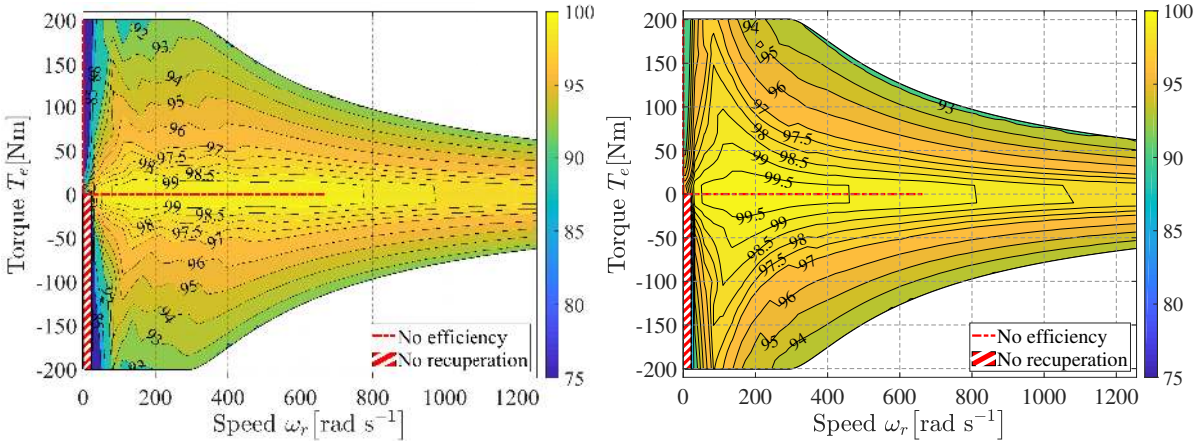

(a) CHB (b) MMSP

Fig. 9: Battery efficiency maps for the (a) CHB and (b) MMSP inverter setup.

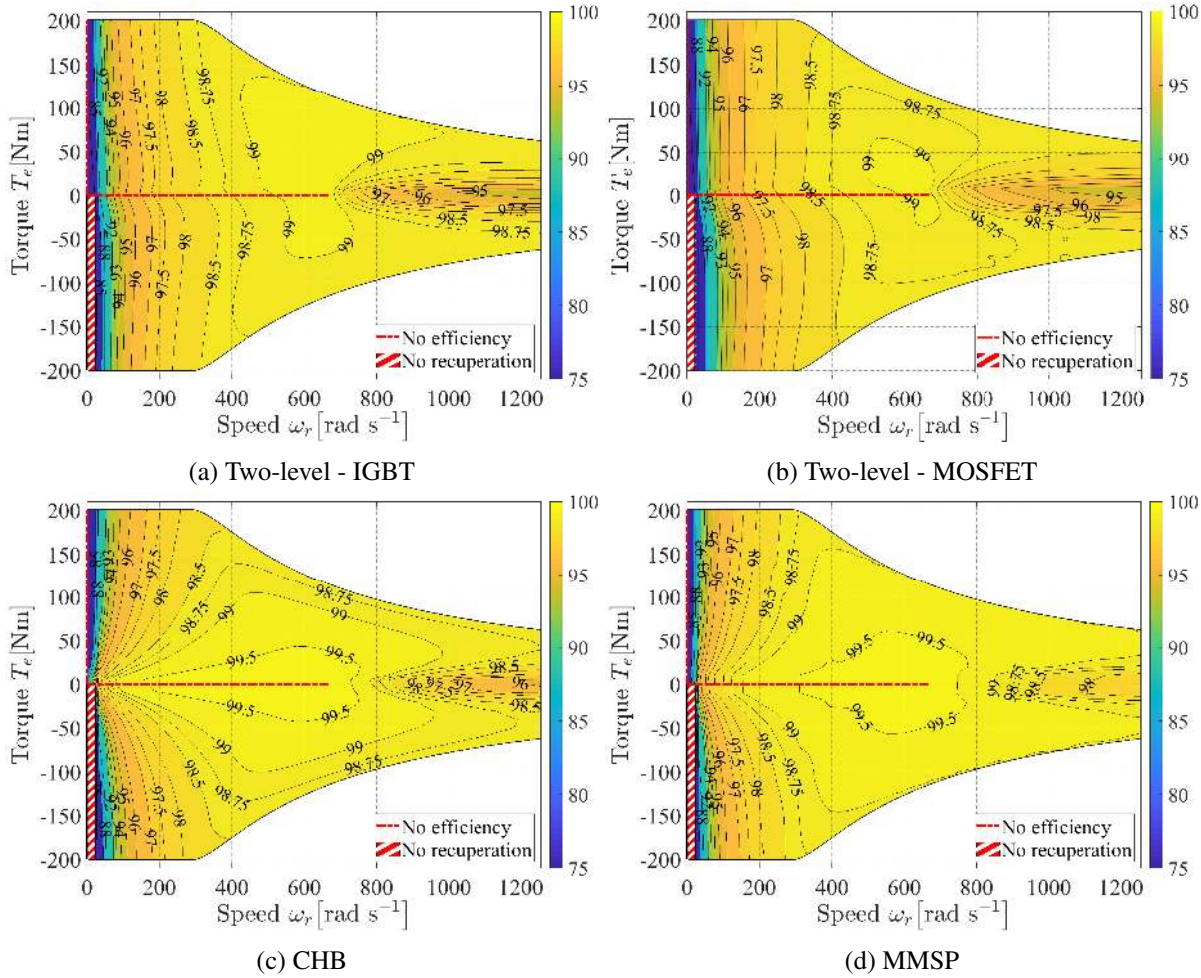

(a) Two-level - IGBT (b) Two-level - MOSFET

(c) CHB (d) MMSP

Fig. 10: Inverter efficiency maps for the (a) two-level IGBT, (b) two-level MOSFET, (c) CHB and (d) MMSP setup at $T_\mathrm{J} = 70\,^\circ\mathrm{C}$.

verter systems. It can be seen that the two-level MOSFET inverter shows the lowest efficiency for any operating point.

Drive Cycle Performance

Within this section the obtained drive cycle results are given, while a greater emphasis is given to the WLTP driving cycle, since it is a global standard for determining emission values and fuel consumption.

Figs. 11(a) and 11(b) show the battery and inverter losses of the different inverter setups during

the WLTP driving cycle. It can be seen that the battery losses are about three times as high as the inverter losses. The obtained junction temperatures, utilizing the previously described thermal models, for the

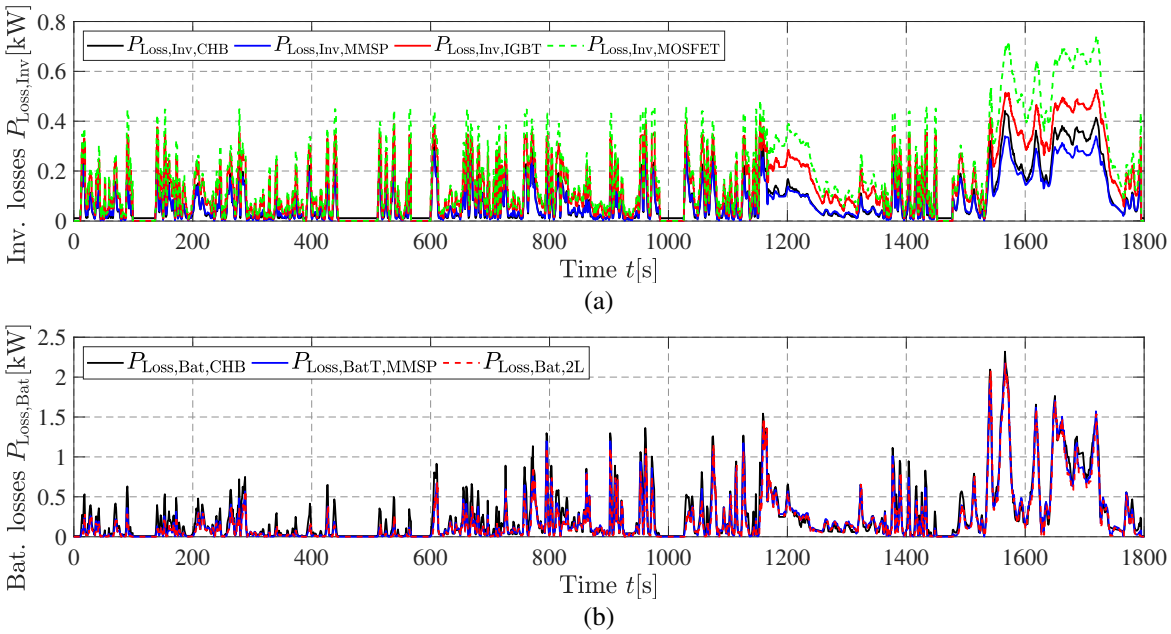

Fig. 11: Comparison of the (a) battery and (b) inverter losses for the WLTP driving cycle.

WLTP driving cycle are shown in Fig. 12. The CHB and the MMSP inverter achieve a redcued junction temperature compared to the MOSFET and the IGBT two-level inverter systems. Finally, Table IV shows

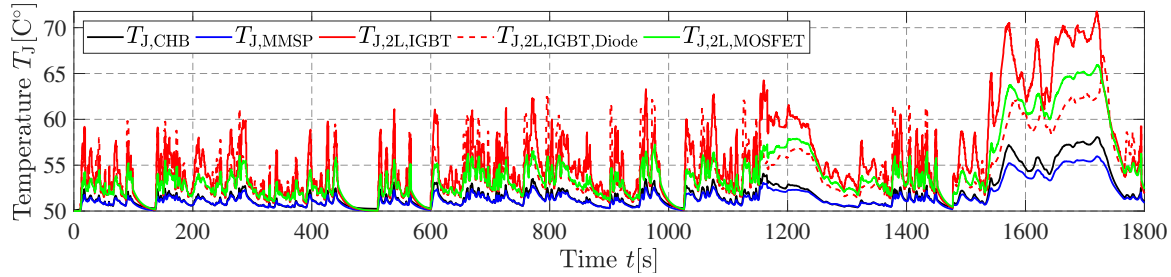

Fig. 12: Junction temperatures of the semiconductor switches during the WLTP driving cycle.

the obtained overall energy losses for the WLTP driving cycle. Here, the MMSP and the CHB show the

Table IV: WLTP - Drive cycle evaluation

	2-L (IGBT)	2-L (MOSFET)	CHB	MMSP
BEV consumption [kWh]	2.9303	2.9492	2.9309	2.9057
Electrical load [kWh]	2.7614	2.7614	2.7614	2.7614
Conduction losses [kWh]	0.0499	0.0211	0.0364	0.0250
Switching losses [kWh]	0.0206	0.0684	0.0053	0.0119
Inverter losses [kWh]	0.0706	0.0895	0.0416	0.0369
Inverter efficiency [%]	97.51	96.86	98.52	98.68
Battery losses [kWh]	0.0983	0.0983	0.1279	0.1074
Battery efficiency [%]	96.65	96.67	95.64	96.31
Overall losses [kWh]	0.1689	0.1878	0.1695	0.1443
Overall efficiency [%]	94.24	93.63	94.22	95.03

highest inverter efficiency, whereas the battery efficiency is decreased in comparison to two-level inverter systems. Regarding the combined drive cycle efficiency, it can be seen that the MMSP inverter achieved

the best result. The CHB inverter is competitive with the chosen two-level IGBT inverter system, whereas the two-level MOSFET inverter system shows the worst result.

Table V shows the obtained efficiency results for the Artemis 130, the NDEC and the FTP-75 driving cycles. The results of Artemis and NEDC are similar to that of the WLTP. However, during FTP75, the CHB inverter shows the worst result.

Table V: Drive cycle evaluation

(a) Artemis 130 (Highway)

	2-L (IGBT)	2-L (MOSFET)	CHB	MMSP
BEV consumption [kWh]	5.2456	5.2824	5.2437	5.2166
Electrical load [kWh]	4.9310	4.9310	4.9310	4.9310
Conduction losses [kWh]	0.0688	0.0384	0.0654	0.0446
Switching losses [kWh]	0.0334	0.1007	0.0070	0.0150
Inverter losses [kWh]	0.1022	0.1391	0.0724	0.0597
Inverter efficiency [%]	97.97	97.26	98.55	98.80
Battery losses [kWh]	0.2124	0.2124	0.2403	0.2259
Battery efficiency [%]	95.95	95.98	95.42	95.67
Overall losses [kWh]	0.3146	0.3514	0.3127	0.2856
Overall efficiency [%]	94.00	93.35	94.04	94.53

(b) NEDC (New European Driving Cycle)

	2-L (IGBT)	2-L (MOSFET)	CHB	MMSP
BEV consumption [kWh]	1.1743	1.1816	1.1702	1.1617
Electrical load [kWh]	1.1105	1.1105	1.1105	1.1105
Conduction losses [kWh]	0.0227	0.0082	0.0141	0.0099
Switching losses [kWh]	0.0088	0.0305	0.0026	0.0057
Inverter losses [kWh]	0.0315	0.0387	0.0167	0.0155
Inverter efficiency [%]	97.24	96.63	98.52	98.62
Battery losses [kWh]	0.0323	0.0323	0.0430	0.0357
Battery efficiency [%]	97.25	97.27	96.32	96.93
Overall losses [kWh]	0.0638	0.0710	0.0597	0.0512
Overall efficiency [%]	94.57	93.99	94.90	95.59

(c) FTP-75 (city)

	2-L (IGBT)	2-L (MOSFET)	CHB	MMSP
BEV consumption [kWh]	1.0840	1.0921	1.0923	1.0705
Electrical load [kWh]	1.0112	1.0112	1.0112	1.0112
Conduction losses [kWh]	0.0294	0.0112	0.0199	0.0136
Switching losses [kWh]	0.0107	0.0371	0.0030	0.0074
Inverter losses [kWh]	0.0401	0.0483	0.0229	0.0210
Inverter efficiency [%]	96.18	95.44	97.78	97.96
Battery losses [kWh]	0.0326	0.0326	0.0581	0.0382
Battery efficiency [%]	96.99	97.01	94.68	96.43
Overall losses [kWh]	0.0728	0.0809	0.0810	0.0592
Overall efficiency [%]	93.29	92.59	92.58	94.47

Conclusion

This paper presents a drive cycle comparison of two-level inverter systems, utilizing IGBTs or MOSFETs, and two seven-level inverters, a CHB and an MMSP inverter, utilizing low voltage MOSFETs.

From the efficiency maps at constant junction temperature, it has been seen that the MOSFET

multilevel inverters showed a high inverter efficiency at partial loading and their peak efficiency was increased in comparison to the two-level inverter solutions. The MMSP inverter has shown a slightly higher efficiency than the CHB inverter. On the contrary, the classical two-level inverter has shown the best result regarding battery efficiency, especially at low speed. Since the phase current is intermittently conducted through the battery packs in the multilevel inverters, the battery losses are increased in comparison to the two-level inverter system. The MMSP inverter reduces the battery losses below rated speed compared to the CHB inverter, whereas the losses at high speed were just marginally affected.

Using different drive cycles as the weighting of the inverter and battery losses, it has been seen that the MMSP inverter achieved the best overall efficiency for all four selected driving cycles. The efficiency of the CHB inverter system was competitive with the two-level IGBT solution for three of the chosen driving cycles. The IGBT two-level inverter was better than the CHB inverter only for the city cycle FTP75. Furthermore, it was seen that using a two-level inverter system with MOSFETs is not a suitable solution, neither from a cost nor efficiency perspective.

References

[1] E. A. Grunditz and T. Thiringer, "Performance analysis of current bevs based on a comprehensive review of specifications," *IEEE Transactions on Transportation Electrification*, vol. 2, no. 3, pp. 270–289, Sep. 2016.

[2] E. Arfa Grunditz and T. Thiringer, "Characterizing bev powertrain energy consumption, efficiency, and range during official and drive cycles from gothenburg, sweden," *IEEE Transactions on Vehicular Technology*, vol. 65, no. 6, pp. 3964–3980, June 2016.

[3] O. Josefsson, T. Thiringer, S. Lundmark, and H. Zelaya, "Evaluation and comparison of a two-level and a multilevel inverter for an ev using a modulized battery topology," in *IECON 2012 - 38th Annual Conference on IEEE Industrial Electronics Society*, Oct 2012, pp. 2949–2956.

[4] A. Kersten, E. Grunditz, and T. Thiringer, "Efficiency of active three-level and five-level npc inverters compared to a two-level inverter in a vehicle," in *2018 20th European Conference on Power Electronics and Applications (EPE'18 ECCE Europe)*, Sep. 2018, pp. P.1–P.9.

[5] O. Josefsson, A. Lindskog, S. Lundmark, and T. Thiringer, "Assessment of a multilevel converter for a phev charge and traction application," in *The XIX International Conference on Electrical Machines - ICEM 2010*, Sep. 2010, pp. 1–6.

[6] F. Chang, O. Ilina, O. Hegazi, L. Voss, and M. Lienkamp, "Adopting mosfet multilevel inverters to improve the partial load efficiency of electric vehicles," in *2017 19th European Conference on Power Electronics and Applications (EPE'17 ECCE Europe)*, Sept 2017, pp. P.1–P.13.

[7] F. Chang, O. Ilina, M. Lienkamp, and L. Voss, "Improving the overall efficiency of automotive inverters using a multilevel converter composed of low voltage si mosfets," *IEEE Transactions on Power Electronics*, vol. 34, no. 4, pp. 3586–3602, April 2019.

[8] O. Josefsson, *Investigation of a Multilevel Inverter for Electric Vehicle Applications*. Doctoral Thesis at Chalmers University of Technology, Gothenburg, Sweden, 2016.

[9] A. Kersten, K. Oberdieck, A. Bubert, M. Neubert, E. Grunditz, T. Thiringer, and R. W. De Doncker, "Fault detection and localization for limp home functionality of three-level npc inverters with connected neutral point for electric vehicles," *IEEE Transactions on Transportation Electrification*, pp. 1–1, 2019.

[10] C. Korte, E. Specht, M. Hiller, and S. Goetz, "Efficiency evaluation of mmspc/chb topologies for automotive applications," in *2017 IEEE 12th International Conference on Power Electronics and Drive Systems (PEDS)*, Dec 2017, pp. 324–330.

[11] A. Acquaviva and T. Thiringer, "Energy efficiency of a sic mosfet propulsion inverter accounting for the mosfet's reverse conduction and the blanking time," in *2017 19th European Conference on Power Electronics and Applications (EPE'17 ECCE Europe)*, Sept 2017, pp. P.1–P.9.

[12] Y. Cao, R. C. Kroeze, and P. T. Krein, "Multi-timescale parametric electrical battery model for use in dynamic electric vehicle simulations," *IEEE Transactions on Transportation Electrification*, vol. 2, no. 4, pp. 432–442, Dec 2016.

[13] F. Helling, M. Kuder, A. Singer, S. Schmid, and T. Weyh, "Low voltage power supply in modular multilevel converter based split battery systems for electrical vehicles," in *2018 20th European Conference on Power Electronics and Applications (EPE'18 ECCE Europe)*, Sep. 2018, pp. P.1–P.10.

[14] LG Chem, "Product Description: ICR18650 C2 2800mAh," https://www.batteryspace.com/prodspecs/5702_5.pdf, (Accessed on 05/04/2019).

[15] E. Grunditz, *Design and Assessment of Battery Electric Vehicle Powertrain, with Respect to Performance, Energy Consumption and Electric Motor Thermal Capability*. Doctoral Thesis at Chalmers University of Technology, Gothenburg, Sweden, 2016.

[16] A. Rabiei, T. Thiringer, M. Alatalo, and E. A. Grunditz, "Improved maximum-torque-per-ampere algorithm accounting for core saturation, cross-coupling effect, and temperature for a pmsm intended for vehicular applications," *IEEE Transactions on Transportation Electrification*, vol. 2, no. 2, pp. 150–159, June 2016.

[17] A. Rabiei, T. Thiringer, and J. Lindberg, "Maximizing the energy efficiency of a pmsm for vehicular applications using an iron loss accounting optimization based on nonlinear programming," in *2012 XXth International Conference on Electrical Machines*, Sep. 2012, pp. 1001–1007.

[18] A. Holm, *SiC converter for electrical vehicle - DC-link ripple*. Master Thesis at Chalmers University of Technology, Gothenburg, Sweden, 2016.

[19] Digi-Key, "EKZN101ELL102MM40S Capacitor - United Chemi-Con," https://www.digikey.de/product-detail/de/united-chemi-con/EKZN101ELL102MM40S/565-4153-ND/4843963, (Accessed on 05/04/2019).

[20] AAVID, "Hi-Contact 6-Pass Cold Plate," https://www.shopaavid.com/images/Product/images/Hi-Contact%206-Pass%20Datasheet_September%202018_A02.pdf, (Accessed on 05/05/2019).

[21] Mouser Germany, "FS400R07A3E3 IGBT Module - Infineon Technologies," https://www.mouser.de/ProductDetail/Infineon-Technologies/FS400R07A3E3?qs=sGAEpiMZZMshyDBzk1%2FWi9eRZbMS8egi7PbmlBZW4DTd0qnoL8YeOA%3D%3D, (Accessed on 05/04/2019).

[22] ——, "FCH023N65S3L4 MOSFET - Fairchild," https://eu.mouser.com/ProductDetail/ON-Semiconductor-Fairchild/FCH023N65S3L4?qs=%2Fha2pyFaduhaggngXRJlxNPoYnp%252BiEMqcVLIm9M9%2FdVGGrPMuKGXQw%3D%3D, (Accessed on 05/04/2019).

[23] Mouser Europe, "C5D50065D Wolfspeed SiC Schottky Diode - Cree Inc." https://eu.mouser.com/ProductDetail/Wolfspeed-Cree/C5D50065D?qs=%2Fha2pyFaduhmv9sDnjvt0d4PibSrCOZu4tH6R9zmXNLYhtvHf1W9og==, (Accessed on 05/09/2019).

[24] Mouser Germany, "IPT015N10N5 MOSFET - Infineon Technologies," https://eu.mouser.com/ProductDetail/Infineon-Technologies/IPT015N10N5ATMA1?qs=%2Fha2pyFadugSmf5FOGPdgNsXqw1rki1BxHCGVLKn37y3DCJRwbhxeg%3D%3D, (Accessed on 05/05/2019).